IOP Publishing | International Atomic Energy Agency Nuclear Fusion

Nucl. Fusion **61** (2021) 066007 (13pp) https://doi.org/10.1088/1741-4326/abf0dd

Gyrokinetic simulation of low-frequency Alfvénic modes in DIII-D tokamak

G.J. Choi[1,*], P. Liu[1], X.S. Wei[1], J.H. Nicolau[1], G. Dong[2], W.L. Zhang[3], Z. Lin[1,*], W.W. Heidbrink[1] and T.S. Hahm[4]

[1] Department of Physics and Astronomy, University of California, Irvine, CA 92697, United States of America
[2] Princeton Plasma Physics Laboratory, Princeton, NJ 08540, United States of America
[3] Institute of Physics, Chinese Academy of Sciences, Beijing, 100190, China
[4] Department of Nuclear Engineering, Seoul National University, Seoul 151-742, Korea, Republic of

E-mail: gyungjic@uci.edu and zhihongl@uci.edu

Received 18 January 2021, revised 11 March 2021
Accepted for publication 22 March 2021
Published 23 April 2021

Abstract

Global gyrokinetic simulations find that a beta-induced Alfvén eigenmode (BAE) and a low-frequency mode (LFM) co-exist in the DIII-D tokamak experiments. The simulated LFM mode structure and many of its parametric dependencies are consistent with experimental observations. The LFM can be excited without fast ions and has a frequency inside the gap of the beta-induced Alfvén-acoustic eigenmode (BAAE). However, an antenna scan shows that it is NOT the conventional BAAE. Instead, the LFM is an interchange-like electromagnetic mode excited by non-resonant drive of pressure gradients. Furthermore, the simulated BAE mode structure is consistent with the experiment but the frequency is lower than the experiment. The compressible magnetic perturbations significantly increase the growth rates of the BAE and LFM. On the other hand, trapped electrons and equilibrium current have modest effects on the BAE and LFM.

Keywords: Alfvén eigenmode, energetic particle, electromagnetic instability, gyrokinetic simulation

(Some figures may appear in colour only in the online journal)

1. Introduction

In magnetic confinement fusion devices, energetic particles (EPs) supplied from neutral beam injection (NBI) or fusion reaction are essential in auxiliary or self-heating for high-performance operation. Alfvén eigenmodes (AEs) are generally regarded as the primary driver for EP transport [1, 2]. They exist in a frequency gap between neighboring continua, where continuum damping is absent so that EP drive can easily excite a mode. The AEs in the toroidicity-induced gap (TAE) [3, 4] and higher frequency gaps have been extensively studied. On the other hand, there has been less attention to the AEs in the beta-induced low-frequency gaps: beta-induced AE (BAE) [5, 6] and beta-induced Alfvén-acoustic eigenmode (BAAE) [7–9]. It was noted that simple fluid theories cannot fully explain the excitation of the BAE [10]. Kinetic theories [11–13] suggest that kinetic thermal ion gap [14, 15] is more relevant for describing low-frequency modes (LFMs) below the BAE range, rather than the magnetohydrodynamic (MHD) BAAE gap. It appears to be more controversial identifying the BAAE and explaining observed features in experiments. An example of the ambiguity for the origin of the modes excited inside the BAAE gap is the 'LFMs' described in reference [16].

In recent DIII-D tokamak L-mode experiments, multiple sub-TAE low-frequency AEs have been observed [17, 18]. Figure 1 shows a spectrogram from interferometer data for the DIII-D shot #178631, where robust activities of the BAE and LFM, together with higher frequency reversed shear AE (RSAE), are observed in the current ramp-up phase with deuterium NBI. Follow-up experiments found that, surprisingly,

* Authors to whom any correspondence should be addressed.

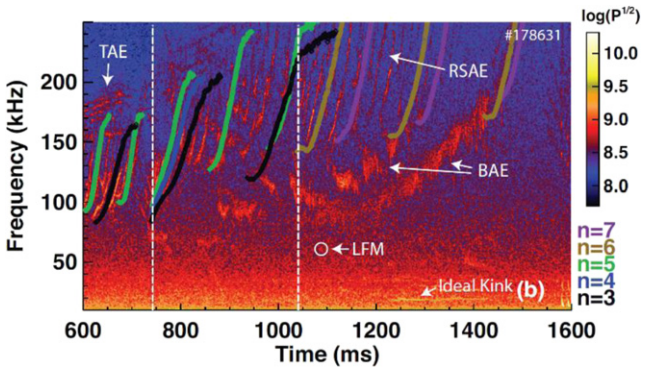

Figure 1. Spectrogram from interferometer data presented in figure 4 for DIII-D discharge #178631 showing multiple low-frequency AE activities. Reproduced courtesy of IAEA. Figure adapted from [17]. Copyright 2021 IAEA.

the LFM persists for a long time after the NBI is turned off and the RSAE and BAE disappear [17]. Detailed experimental measurements of the BAE and LFM appear in references [17, 18], respectively. Reference [17] concludes that the LFM is not the theoretical BAAE, but a LFM having characteristics of a low frequency Alfven mode. On the other hand, the experimental BAE is driven by the fast ions and has a frequency close to the BAE accumulation point of the MHD continuous spectrum [18].

In this work, for physics identification and understanding of the BAE and LFM observed in the experiments, we perform first-principle linear simulation study of the DIII-D shot #178631 using global gyrokinetic toroidal code (GTC) [19], which has been extensively verified and validated for AE simulations [20–22] and applied for physics study of low-frequency AEs [23–29]. In particular, earlier GTC simulations of a tokamak with concentric cross-section find that BAAE and BAE can be simultaneously excited with comparable linear growth rates even though damping rate of BAAE is much larger than BAE in the absence of EPs [27].

In the current work, linear GTC simulations using realistic magnetic geometry and plasma profile of the DIII-D tokamak shot #178631 first found that the LFM can be excited without fast ions and has a frequency inside the gap of the BAAE, consistent with the experimental observation in reference [17]. However, the physics interpretation of the LFM was still unclear at that time since no eigenmode in the BAAE gap was found in the GTC antenna scan. Then, an important breakthrough came from the GTC simulation that found, for the first time, that the LFM is excited by the non-resonant drive of pressure gradients. Subsequently, detailed analyses of the mode structure and polarization from the simulation led us to conclude that the LFM is an interchange-like electromagnetic mode. These simulation results provided the physics insights for the interpretation of the experimental observations of the LFM and the associated deployment of the theoretical model as reported in reference [17]. Finally, GTC simulations found that compressible magnetic perturbations significantly increase the growth rates of the LFM and BAE, a surprising result that took us through a lengthy process to verify by carefully examining GTC formulation and simulation results.

This paper is organized as follows. In section 2, we present the primary results of GTC simulations of BAE and LFM in the DIII-D #178631 showing that the LFM inside the BAAE gap can be excited without fast ions. In section 3, we present mode polarization properties. In section 4, we present the results of energy exchange analysis which reveals that LFM is reactively excited. In section 5, we present various parameter scans. In section 6, we compare BAE and LFM from linear GTC simulations with experimental measurements. The paper closes by summarizing key results of the simulations, listing points of agreement and disagreement between simulation results and experimental measurements, and outlining future work (section 7).

2. Linear dispersion and mode structure

First, we describe simulation model and input parameters used in GTC simulations. The linear electromagnetic global δf gyrokinetic simulations use gyrokinetic fast and thermal ions and fluid-kinetic hybrid electrons [30, 31], with initial Maxwellian distribution for all species. We neglect collisions and toroidal rotation in the simulation, but add Doppler-shift to frequencies of the BAE and LFM from simulations when comparing experimental measurements [32, 33]. We include perturbed compressible magnetic field ($\delta B_\parallel$) in simulations [34]. GTC simulations use experimental equilibrium and profile [35] as shown in figure 2 for the DIII-D shot #178631 at the time $t = 1200$ ms, obtained by the equilibrium fitting (EFIT) reconstruction [36]. Important on-axis parameters are $n_{ea} = 4.05 \times 10^{19}$ m^{-3}, $T_{ea} = 4.15$ keV, $B_a = 2.0$ T, $a = 0.64$ m and $R_0 = 1.65$ m. The q-profile has a reversed shear configuration with $q_{min} = 1.33$. The relaxed fast ion profile provided with EFIT reconstruction is used for comparison to the case with the classical fast ion profile obtained using TRANSP/NUBEAM [37, 38]. The true fast ion profile likely lies between these two extreme cases. For simulations, we use $100 \times 200 \times 24$ grids in radial, poloidal and parallel directions, respectively. Particle number per cell is 1000 for each species. We simulate an $n = 3$ BAE and an $n = 6$ LFM to compare with experimental measurements, since they are representative BAE and LFM observed in the experiment. For a physics study, we simulate and compare the $n = 3$ BAE with an $n = 3$ LFM. Since $1.3 < q_{min} < 1.4$, we keep only poloidal harmonics $m \in [n, 2n]$ for each single-n simulation focusing on $m \approx nq_{min}$.

We find from these linear GTC simulations that an unstable BAE and a LFM in the BAAE frequency gap co-exist in the DIII-D #178631. The LFM is excited in the simulation without the fast ions. In the simulations with the fast ions, BAE is strongly excited. Figure 3 shows an overview of these low frequency Alfvénic modes, together with ideal MHD continua calculated by an ideal MHD eigenvalue solver ALCON [39]. Taking into account geodesic compressibility and contribution from adiabatic fast ions, we use an effective MHD pressure as input for ALCON as follows:

$$P_{eff} = P_e + \frac{7}{4}\frac{P_i}{1 - n_f/n_e}. \quad (1)$$

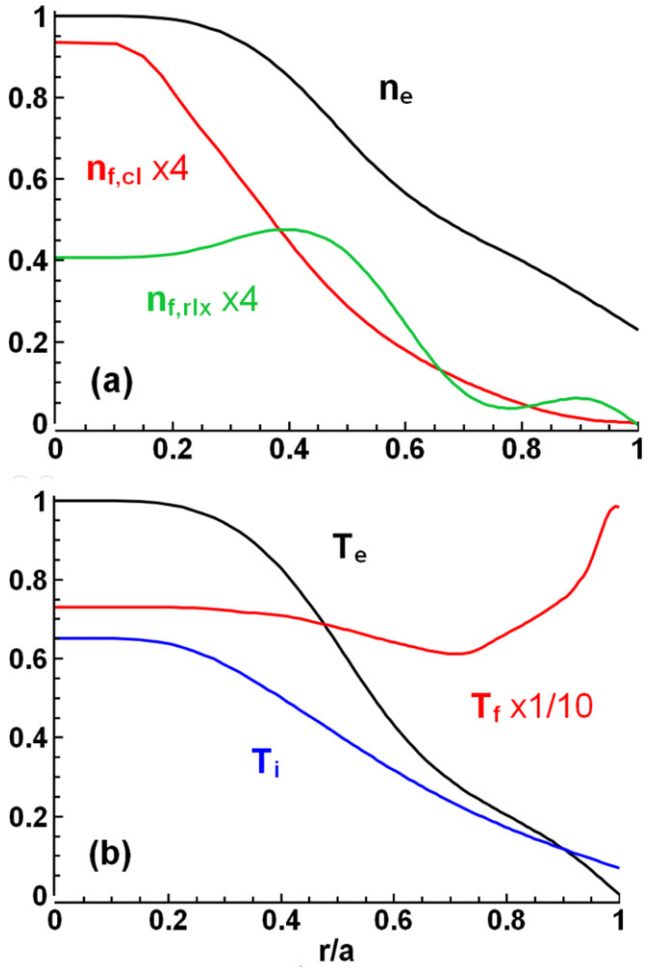

Figure 2. Radial profiles of (*a*) density and (*b*) temperature of DIII-D #178631 used for GTC simulations, normalized by on-axis electron density and temperature, respectively.

Here, $P_{\mathrm{e,i}}$ are electron and thermal ion pressures and $n_{\mathrm{f,e}}$ are fast ion and electron densities, respectively. Note that the low-frequency MHD continua calculated for the case without the fast ions show only small quantitative difference from figure 3. We emphasize that LFM is not a conventional AE driven by the fast ions, and hereafter LFM in this paper is always from simulations without fast ions. The result is consistent with observations in the follow-up DIII-D experiments [17], where BAAE activity persist for a long-time after the NBI is turned off. GTC finds no unstable $n = 3$ mode from linear electrostatic simulations, with or without fast ions. It indicates that the LFMs observed in these DIII-D experiments are not electrostatic modes. Both BAE and LFM propagate in the direction of ion diamagnetic drift [15, 16].

Note that LFM is closer to the q_{min} surface than the BAE. In figure 3, the full-width-half-maximum of the radial mode structures of the BAE and LFM are marked by double-sided arrows. BAE is located near the radial location of the $m = 4$ BAE accumulation point. The location of the LFM is closer to the $q = 4/3$ surface. Note that the BAE frequency = 57 kHz with the classical fast ion profile is lower in the BAE gap than the BAE with the relaxed fast ion profile. Linear growth rates of the BAE with classical and relaxed fast ion profiles are,

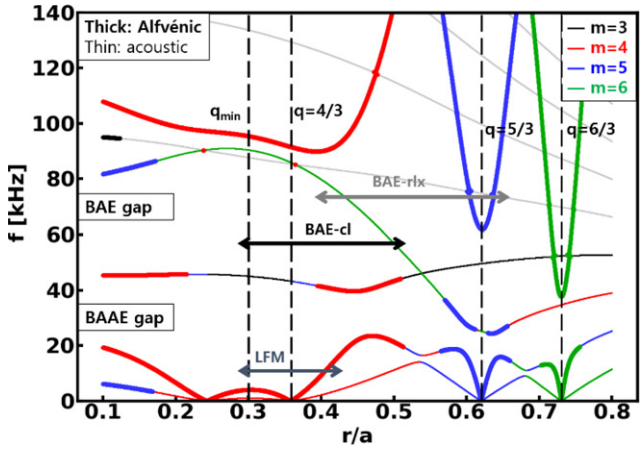

Figure 3. Frequency and radial widths of unstable $n = 3$ BAE and $n = 3$ LFM from linear GTC simulations, together with ALCON plot of $n = 3$ MHD continua in the plasma frame. BAE-cl and BAE-rlx denote BAE excited by classical and relaxed fast ion profiles, respectively.

respectively, $\gamma/2\pi = 5.4 \times 10^4\ \mathrm{s}^{-1}$ and $2.8 \times 10^4\ \mathrm{s}^{-1}$, and that of the LFM is $1.4 \times 10^4\ \mathrm{s}^{-1}$. Ratios of the linear growth rate to the frequency are $\gamma/\omega = 0.95$, 0.38 and 1.0, respectively. Large values of $\gamma/\omega \sim \mathcal{O}(1)$ indicate that there can be either a broad wave–particle resonance or a strong non-resonant drive for both unstable BAE and LFM. The simulated BAE linear eigenmode structure using the classical fast ion profile is closer to the measured mode structure than that using the relaxed fast ion profile, so we mainly use the classical fast ion profile in this paper.

Figure 4 shows 2D structures of electrostatic potentials in the poloidal planes. Mode structure of the BAE is more ballooning with multiple poloidal harmonics m and that of the LFM is more interchange-like dominated by a single poloidal harmonic $m \approx nq$. The contours of the BAE have a triangular shape, while those of the LFM have an elliptic one. In general, it is known to be due to the non-perturbative fast ion effects [1, 20, 21, 40–42], either by fast ion non-uniformity or fast ion–wave interaction. The 2D poloidal mode structures in figure 4 are consistent with the radial profiles of poloidal harmonics of the electrostatic potential in figure 5. For both the BAE and LFM, the primary poloidal harmonic is $m = 4$. Contribution from sidebands ($m = 3$, 5, 6) to the LFM is weaker than that to the BAE, consistent with its weaker ballooning character.

3. Polarization

For electrostatic perturbations such as ion acoustic wave (IAW) and drift wave (DW), the parallel electric field $E_{\parallel}$ only contains an electrostatic component $E_{\parallel,\mathrm{ES}}$ due to the perturbed electrostatic potential, i.e., $E_{\parallel} = E_{\parallel,\mathrm{ES}}$. On the other hand, $E_{\parallel} = 0$ for Alfvénic waves in the ideal MHD state due to the cancellation between the electrostatic component and the inductive component, which can be broken by resistivity, electron inertia, wave–particle interaction, finite-Larmor-radius effect, and toroidicity [1]. Coupling of the

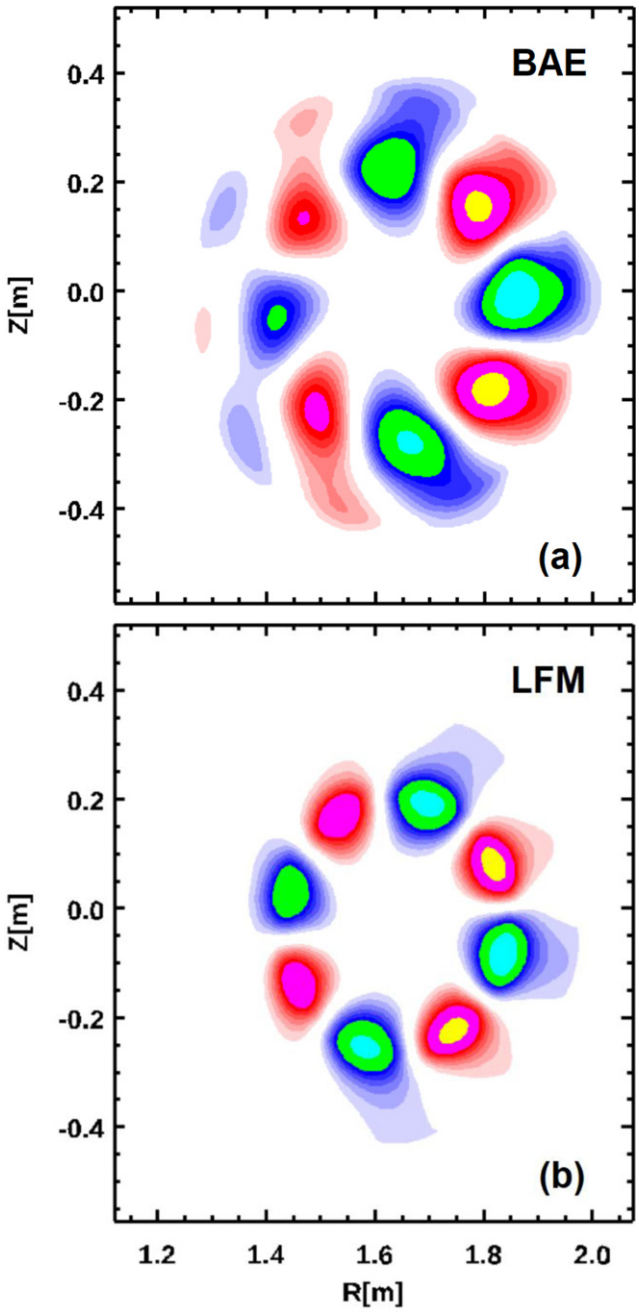

Figure 4. Two-dimensional structure of electrostatic potential ϕ of (a) BAE and (b) LFM on the poloidal plane. Periodic change from positive (red) to negative (blue) values in poloidal angle shows dominant $m = 4$ harmonic for both BAE and LFM.

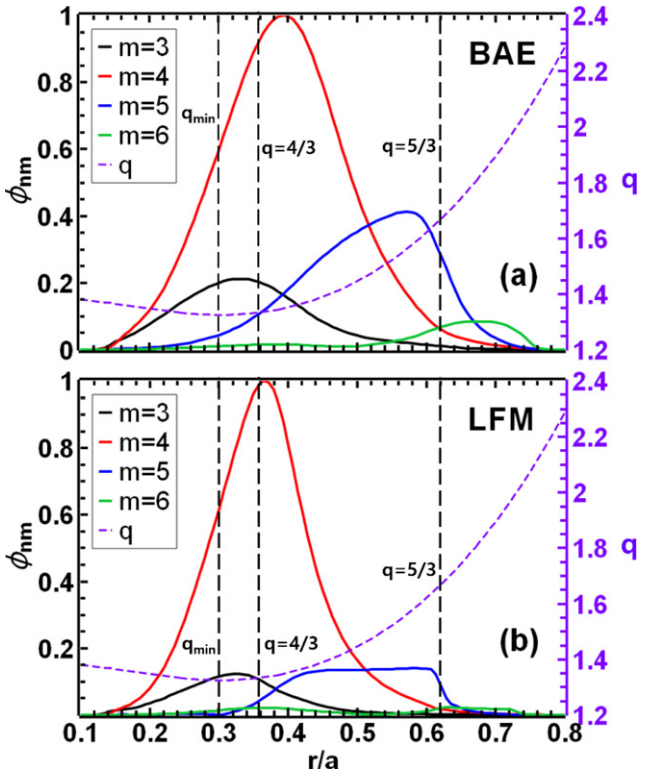

Figure 5. Radial profiles of electrostatic potential ϕ of (a) BAE and (b) LFM for each poloidal harmonic (solid lines), together with q-profile (dashed purple line). The ϕ is normalized by its maximal value of the primary poloidal harmonic. The vertical black dashed lines indicate radial location of various q values.

Alfvén waves with the IAW and DW could also induce finite $E_\parallel$.

We find that the unstable BAE has predominantly Alfvénic polarization while the unstable LFM is relatively more acoustic. Figure 6 shows radial structures of the parallel electric field $E_\parallel$ of the BAE and LFM for each poloidal harmonic. They are normalized by the radial peak of the root-mean-square (rms) of electrostatic component $E_{\parallel,\mathrm{ES}}$. Figure 6 clearly shows that the sidebands carry most of the parallel electric field. The estimated polarization $E_\parallel/E_{\parallel,\mathrm{ES}}$ using volume-average of square of $E_\parallel$ and $E_{\parallel,\mathrm{ES}}$ is 0.10 for the BAE and 0.28 for the LFM, showing that the polarization of the LFM significantly deviates from that of the ideal MHD perturbation. In figure 6, it is obvious that the main poloidal harmonic has a negligible contribution to the parallel electric field compared to the sideband near the mode peak. It is a natural consequence of coupling between the shear Alfvén wave (SAW) and IAW [7, 8], which is crucial for the low frequency gaps [43]. The LFM has more acoustic component compared to the BAE. Note that it is different than the fast ion-driven BAAEs from GTC simulations of a simple tokamak plasma [27], where the polarization of an unstable BAAE is very similar to an unstable BAE.

We have analyzed another polarization property, $\tilde{B}_\parallel/\tilde{B}_\perp$, the ratio of parallel to perpendicular magnetic perturbations. It measures the deviation from shear Alfvénic polarization, as $\tilde{B}_\parallel/\tilde{B}_\perp = 0$ for shear Alfvénic wave while it is finite for fast/slow magnetosonic waves [44]. Figure 7 shows radial profiles of rms of the magnetic perturbations in for the BAE and LFM. The compressible component $\tilde{B}_\parallel$ peaks near the mode rational surface for both the BAE and LFM. Note that the values $\tilde{B}_\parallel/\tilde{B}_\perp \sim 0.5$ in this DIII-D plasma with $\beta = 2.8\%$ are much larger than a typical SAW ordering [1, 45, 46], where $\tilde{B}_\parallel/\tilde{B}_\perp \sim \mathcal{O}(\beta)$. Discussions on the result $\tilde{B}_\parallel/\tilde{B}_\perp \sim \mathcal{O}(1)$ is presented in appendix A with a more precise ordering.

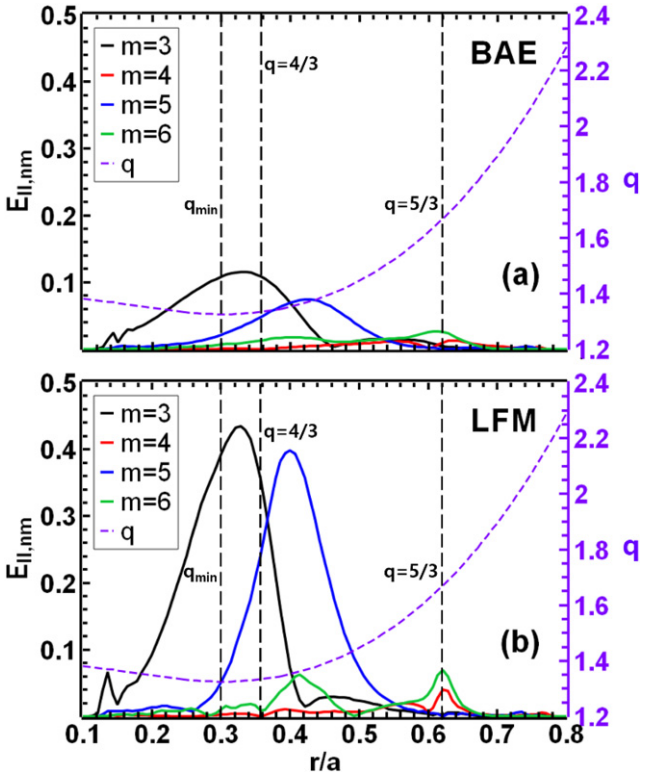

Figure 6. Radial profiles of parallel electric field $E_{||}$ of (*a*) BAE and (*b*) LFM for each poloidal harmonic, together with q-profile. They are normalized by the value at radial peak of rms of the electrostatic part of the parallel electric field $E_{||,\mathrm{ES}}$.

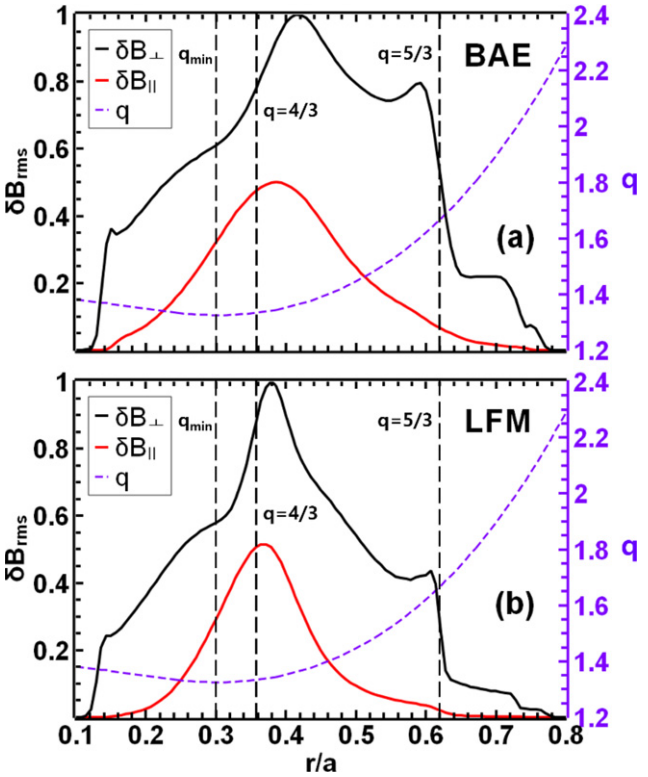

Figure 7. Radial profiles of flux surface-averaged perpendicular (black) and parallel (red) perturbed magnetic fields B_{rms} of (*a*) BAE and (*b*) LFM, together with q-profile. The B_{rms} is normalized by the maximal values of the corresponding perpendicular perturbed magnetic field.

4. Energy exchange

To understand the excitation of the unstable BAE and LFM, we now analyze the wave–particle energy exchanges. We find that the drive of the LFM is mainly non-resonant, interchange type, in contrast to the mostly resonant drive of the BAE. The time rate of energy loss by particles is equivalent to the time rate of change of the wave energy density, since the local energy conservation law holds for a collisionless gyrokinetic system [45, 47, 48]. Therefore, we have [27]

$$\frac{\mathrm{d}\delta W}{\mathrm{d}t} \cong -\sum_{\mathrm{s}} e_{\mathrm{s}} \left[\langle \langle \mathbf{v}_{\perp \mathrm{s}} \cdot \mathbf{E}_{\perp} \rangle_{\mathrm{v}} \rangle + \langle \langle v_{\parallel \mathrm{s}} E_{\parallel} \rangle_{\mathrm{v}} \rangle \right], \qquad (2)$$

where δW is the flux-surface-averaged wave energy density, and the brackets $\langle \cdots \rangle$ and $\langle \cdots \rangle_{\mathrm{v}}$ denote flux-surface-average and gyrocenter velocity space integral weighted by perturbed distribution function, respectively. Here, s is an index for species, e_{s} is charge of the species, and $\mathbf{v}_{\perp \mathrm{s}}$ and $v_{\parallel \mathrm{s}}$ are gyrocenter velocities in the perpendicular and the parallel directions, respectively. Accordingly, the first and the second terms in the right-hand side of equation (2) denote perpendicular and parallel channels of wave–particle energy exchange rate, respectively. Note that they include both non-resonant (fluid) and resonant (kinetic) energy exchanges.

Figure 8 shows radial profiles of the wave–particle energy exchange rates of the BAE and LFM. Overall, the BAE has a wider domain of wave–particle interaction compared to the LFM, which is consistent with the wider width of the mode structure of the BAE shown in figure 3. In figure 8, we use shorthand notations $\mathrm{i}_\perp$, $\mathrm{e}_{\perp,\mathrm{na}}$ and $\mathrm{f}_\perp$ for perpendicular channels (solid lines) and $\mathrm{i}_{||}$, $\mathrm{e}_{||,\mathrm{na}}$ and $\mathrm{f}_{||}$ for parallel channels (dashed lines). Explicit expressions for these notations are presented in appendix B. The nonadiabatic, i.e., the kinetic parts of the wave–electron energy exchange rate ($\mathrm{e}_{\perp,\mathrm{na}}$ and $\mathrm{e}_{||,\mathrm{na}}$) are calculated using the non-adiabatic electron response in the fluid-kinetic hybrid electron model [30]. Meanwhile, the adiabatic component of the electron response is used to calculate the fluid parts of the energy exchange rate, i.e., interchange drive (e_{ic}):

$$\mathrm{e}_{\mathrm{ic}} = \langle \delta P_{\mathrm{e,incomp}} \left(\frac{\mathbf{b}_0 \times \nabla B_0}{B_0^2} + \frac{\nabla \times \mathbf{b}_0}{B_0} \right) \cdot \nabla \phi \rangle, \qquad (3)$$

where $\delta P_{\mathrm{e,incomp}}$ is the incompressible electron pressure perturbation as defined in appendix B. Similarly, we can calculate the interchange drives of the thermal (i_{ic}) and fast (f_{ic}) ions. Note that the total energy exchanges are ($\mathrm{e}_{\mathrm{ic}} + \mathrm{e}_{\perp,\mathrm{na}} + \mathrm{e}_{||,\mathrm{na}}$) for electrons, ($\mathrm{i}_\perp + \mathrm{i}_{||}$) for thermal ions, and ($\mathrm{f}_\perp + \mathrm{f}_{||}$) for fast ions.

Figure 8(*a*) shows that perpendicular resonant wave–fast ion energy exchange is the main drive of the BAE. It suggests the crucial role of bounce-drift fast ion resonance on the BAE excitation. In contrast, figure 8(*b*) shows that the main drive of the LFM is the interchange-type energy exchange. Note that non-interchange contribution from the ion perpendicular

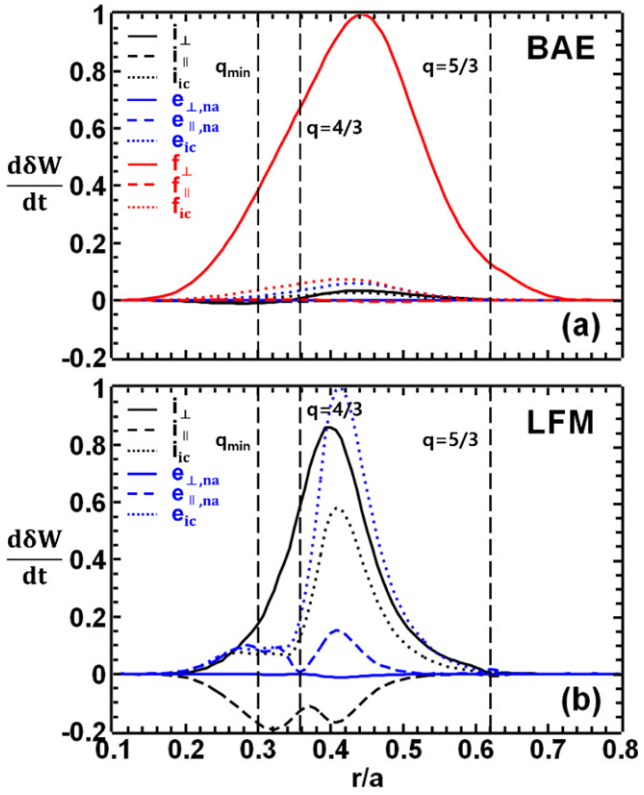

Figure 8. Radial profiles of wave–particle energy exchange rates for (*a*) BAE and (*b*) LFM, in parallel and perpendicular channels of each species, normalized by the maximum amplitude of the dominant one. The subscripts 'na' and 'ic' denote 'non-adiabatic' and 'interchange', respectively.

channel nearly cancels out with that from the ion parallel channel so that the net ion drive is also very close to the ion interchange drive. While figure 8(*a*) shows that there is little energy sink in the BAE, figure 8(*b*) shows that there is a significant energy sink in the LFM due to thermal ion Landau damping [49].

The energy exchange analysis reveals clear non-local aspects for both BAE and LFM. First, for both BAE and LFM, the width of the radial domain of the energy exchanges is on the macroscopic length scale $L_{pi}/a \cong 0.2$. Second, for both BAE and LFM, there is a radial mismatch between local source and sink, indicating a radial energy flux. Third, for BAE, the perpendicular thermal ion channel plays a role of a source in the outer half, while it acts as a sink in the inner half. Fourth, for LFM, the parallel thermal ion channel, which provides the main sink, has double peaks with a dent in the middle. Locations of the peaks coincide with those of the maximal parallel electric field in figure 6. It clearly shows that acoustic sidebands play an important role via ion Landau damping. All these non-local aspects indicate that physics understanding from conventional concepts of a single narrow kinetic layer and an outer ideal MHD region is insufficient for the low-*n* BAEs and LFMs.

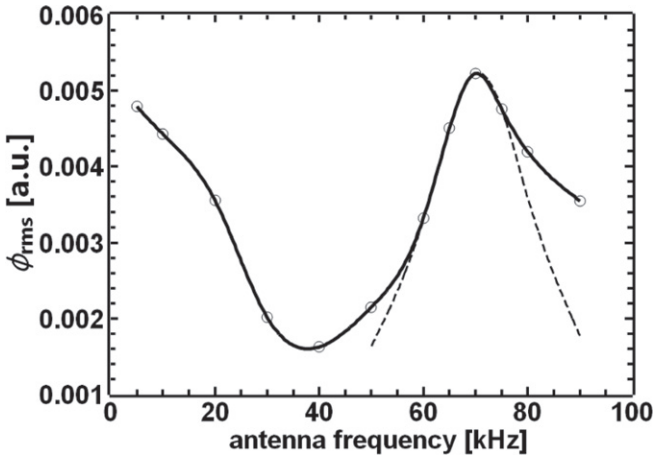

Figure 9. Saturated amplitude (solid line with circles) of electrostatic potential in GTC antenna frequency scan using uniform thermal plasma. Fitting curve (dashed line) shows clear resonance peak of antenna-driven BAE, but there is no clear resonance in low frequency regime.

5. Antenna excitation and parameter scans

In this section, we present GTC simulation results of antenna excitation and parameter scans for linear dispersions of the BAE and the LFM. The antenna scan shows a clear resonance peak for the BAE, but no peak for the LFM. The antenna field

$$A_{\parallel,\mathrm{ant}} = A(\psi)\cos(m\theta - n\zeta)\cos\,\omega t, \tag{4}$$

has a Gaussian envelope $A(\psi)$ peaking at the same radial location of the LFM peak. Here, ψ is poloidal magnetic flux which labels magnetic surface, and θ and ζ are poloidal and toroidal angles, respectively.

Figure 9 shows the result of GTC simulations of antenna-driven mode amplitudes in a uniform thermal plasma. Values of the uniform densities and temperatures were set to be the same as those at the unstable LFM peak. A fitting with a cavity resonance formula [50]

$$\phi^2 \propto \frac{1}{\left(\omega_{\mathrm{ant}} - \omega_{\mathrm{res}} + \gamma_{\mathrm{damp}}\right)^2 + \gamma_{\mathrm{damp}}^2}, \tag{5}$$

shows a clear resonance corresponding to a damped BAE [23] with frequency $f_{\mathrm{res}} = \omega_{\mathrm{res}}/2\pi = 85$ kHz and linear damping rate $\gamma_{\mathrm{damp}}/2\pi = -1.4\times 10^4\ \mathrm{s}^{-1}$. Note that the resonance peak in figure 9 has been down-shifted by an amount of γ_{damp}. Also, the resonance frequency of the antenna-driven BAE is significantly higher than that of the fast ion-driven BAE ~ 57 kHz. It shows that thermal plasma non-uniformity and non-perturbative fast ion effect reduce the BAE frequency. The absence of a lower-frequency resonance peak, in contrast to the previous GTC study of antenna-excited BAAEs [26], implies that LFM excited in the DIII-D discharge #178631 is not a conventional AE. Rather, the LFM is an Alfvénic mode driven by thermal plasma inhomogeneity.

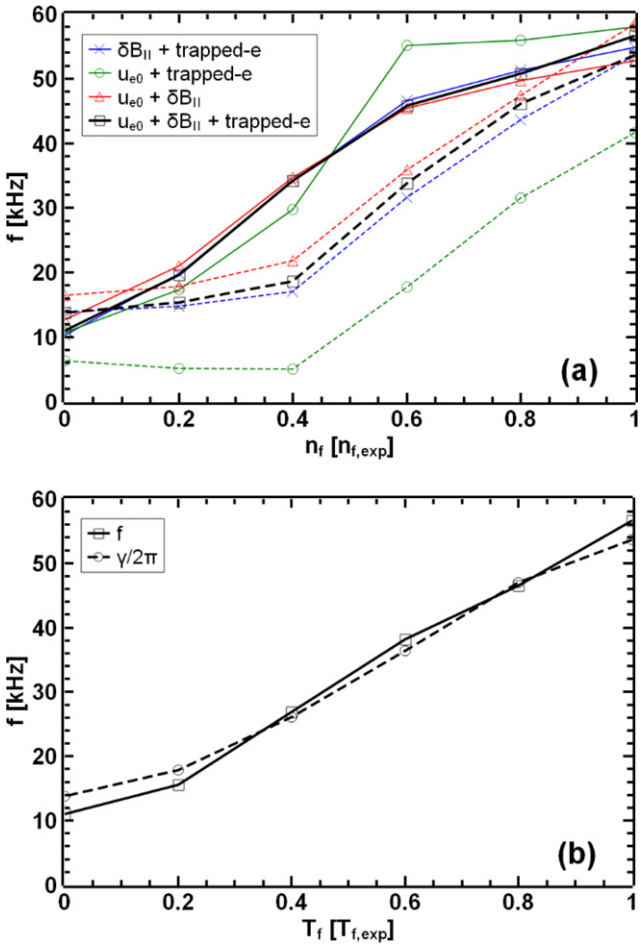

Figure 10. Dependence of real frequencies (solid) and growth rates (dashed) on fast ion (*a*) density and (*b*) temperature for the most unstable mode, which change from LFM to BAE as fast ion pressure gradient increases. Black lines are from the most comprehensive model incorporating most of relevant physics. Blue, green and red lines correspond to the models without kink drive, parallel magnetic compression and kinetic electrons, respectively.

Scans of fast ion density and temperature show continuous change, rather than a sudden transition, of the most unstable mode from the BAE to the LFM. Figure 10(*a*) shows a scan with decreasing fast ion density from the experimental density. Note that the lower fast ion density is relevant to an experimental condition with lower beam power. Meanwhile, a scan with decreasing fast ion temperature in figure 10(*b*) is relevant to the slow thermalization of fast ions after the beams turn off. The simulation without fast ions ($T_f = 0$) describes fully thermalized fast ions. Overall, in figure 10, we find strong non-perturbative effects on the BAE and LFM, leading to a continuous change of the linear dispersion from the BAE to the LFM.

Comparing results in figure 10(*a*) from various simulation models, one can delineate the effects of equilibrium electron current u_{e0} (kink drive in GTC [51, 52]), parallel magnetic perturbation $\delta B_\parallel$ and trapped electrons. The cases with (black lines) and without (blue lines) u_{e0} show that kink drive is weak, as expected. The cases with (black lines) and without (green lines) $\delta B_\parallel$ show that the compressible magnetic perturbation is strongly destabilizing. Also, $\delta B_\parallel$ decreases the BAE frequency. The result is consistent with the cancellation of the drift-reversal stabilization by the compressible magnetic perturbation [34, 53–55] and minimization of the plasma potential energy δW [56, 57]. The cases with (black lines) and without (red lines) kinetic effects from trapped electrons show that their stabilizing role is modest.

Figure 11 shows the dependences of the LFM frequency and linear growth rate on the thermal plasma density and temperature. We find that high electron temperature and density are strongly destabilizing for the LFM. Meanwhile, ion temperature is responsible for the LFM frequency, and higher ion temperature is stabilizing for a given total pressure. The overall feature of these results is consistent with energy exchange analysis, indicating roles of electrons and thermal ions on the LFM stability through the pressure gradient drive and the ion Landau damping. In particular, this is consistent with the DIII-D experiments where LFM excitation has a strong positive correlation with the electron temperature [17].

Note that both BAE and LFM propagate in direction of the ion diamagnetic drift. For the BAE it comes from fast ion resonances. For the LFM frequency, figure 11(*b*) shows that it monotonically increases with ion temperature, indicating ion diamagnetic effect. Electron temperature and density do not change LFM frequency much. In particular, the electron density dependence of LFM frequency is completely different from that of Alfvén frequency, which should decrease with the electron density. It is another evidence that the LFM is not a conventional AE. Figure 11(*c*) shows the results of thermal ion temperature scan keeping the same total pressure by increasing electron temperature accordingly when decreasing ion temperature. The result shows stabilizing role of thermal ions compared to electrons at a given total beta.

We find an ideal interchange/ballooning mode using an incompressible ideal MHD model in GTC. Linear growth rate of the ideal MHD mode with parallel magnetic compression is $\gamma/2\pi = 3.6\times 10^4$ s^{-1}, much higher than 1.8×10^4 s^{-1} for the LFM from the gyrokinetic simulation with a low ion temperature. This is expected from the ideal MHD model without parallel electric field, as there is no ion Landau damping and radiative damping by kinetic SAW. Therefore, the LFM found in linear GTC simulations, theoretical interpretation, and in DIII-D experiments without NBI [17], is basically an interchange-type mode with finite frequency due to ion diamagnetic effects. This is a pressure-driven Alfvénic mode excited inside the kinetic thermal ion gap $(0, \omega_{*\mathrm{pi}})$ reactively, where $\omega_{*\mathrm{pi}}$ is the ion diamagnetic frequency [12–14, 17]. For example, our simulations find that the $n = 3$ LFM frequency is 11 kHz and $\omega_{*\mathrm{pi}} = 15$ kHz at the radial location with the maximal mode amplitude. As a reference, the thermal ion transit, bounce and precession frequencies at the LFM peak locations are, respectively, $\omega_{\mathrm{ti}} \approx 16$ kHz, $\omega_{\mathrm{bi}} \approx 6$ kHz and $n\omega_{\mathrm{pri}} \approx 2$ kHz. Therefore, there can be ion transit resonance as indicated by the wave–particle energy exchanges show in figure 8.

Toroidal mode number n scan shows that the linear growth rates of both BAE and LFM have weak n-dependences. Figures 12(*a*) and (*b*) show the n-scan results of the linear

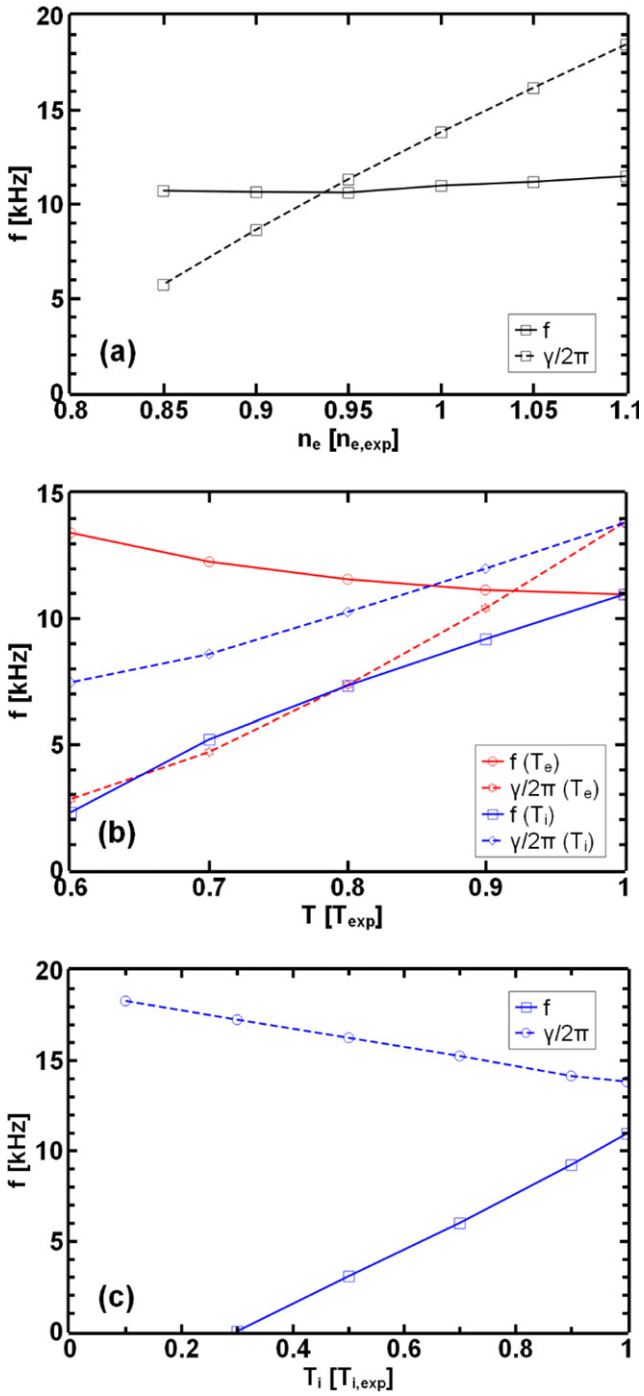

Figure 11. Dependence of LFM real frequencies (solid) and growth rates (dashed) on (*a*) electron density, and (*b*) electron and ion temperatures. Panel (*c*) is an ion temperature scan with fixed total plasma pressure.

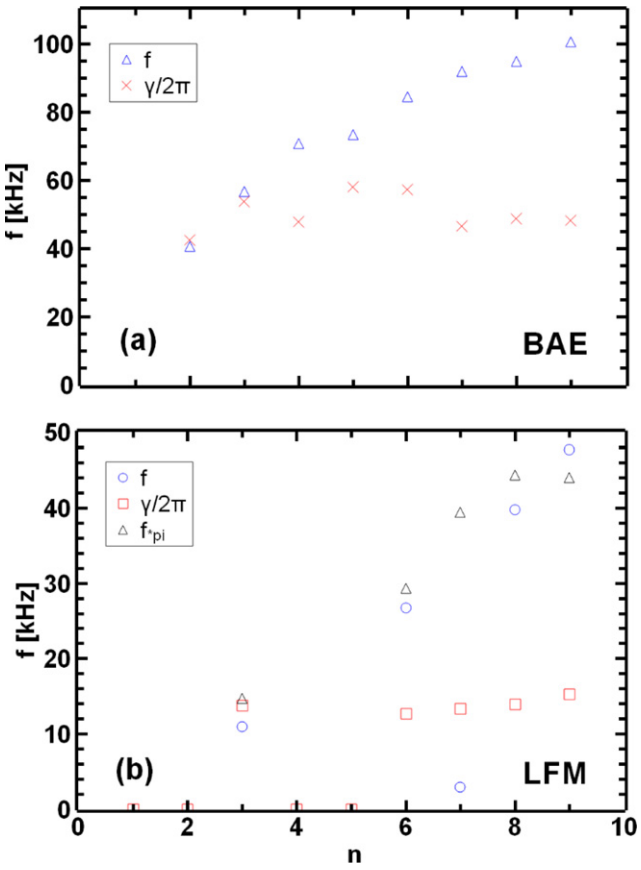

Figure 12. Toroidal mode number n dependence of real frequency (blue) and linear growth rate (red) of (*a*) BAE and (*b*) LFM. Black triangles in panel (*b*) denote ion diamagnetic frequency.

dispersion for the BAE and LFM, respectively. The scaling of the LFM frequency $\sim\omega_{*\mathrm{pi}}$ is consistent with our interpretation that the LFM is an interchange-type mode. Note that in figure 12(*b*), the ion diamagnetic frequency has been estimated at the mode peak location for each n mode. The LFM scaling also indicates that an interpretation with the thermal ion gap with the upper bound $\sim\omega_{*\mathrm{pi}}$ is more appropriate than one with the MHD BAAE gap. Note that there is no drop of LFM linear growth rate when LFM frequency increases across the upper bound of the MHD BAAE gap (see figure 3). The $n = 3$, 6 and 9 LFMs have mode peaks at similar locations and have similar growth rates to each other, even though their mode numbers and frequencies are largely different. This is another indication of the interchange-type mode. The reason for the stable $n = 4$ and 5 LFMs is due to the absence of a mode rational surface near $q_{\min} = 1.325$, where magnetic shear-induced stabilization is weak.

For completeness of the physics identification of the LFM, we have performed linear electrostatic GTC simulations over the range of the toroidal mode numbers in figure 12. Excited electrostatic modes have much smaller linear growth rates than corresponding electromagnetic modes. The electrostatic modes propagate in the electron diamagnetic direction with frequencies similar to trapped electron precessional frequency so they are likely collisionless trapped electron modes.

6. Comparison with experimental measurements

In this section, we discuss the comparison of linear GTC simulation results to experimental measurements in the DIII-D discharge #178631 near 1200 ms. While radial structures from simulations and experimental measurements agree rather well, frequencies show significant differences. Figures 13(*a*) and (*b*)

show the radial structures of the electron temperature perturbation normalized by the local equilibrium temperature, $\delta T_e/T_{e0}$, obtained from linear GTC and electron cyclotron emission (ECE) measurements. Note that for the comparison, $\delta T_e/T_{e0}$ from the linear GTC and the ECE have been further normalized by their values at radial peak. In the simulations, $\delta T_e/T_{e0}$ is estimated using the adiabatic (incompressible) electron temperature response as follows

$$\delta T_e \simeq -\boldsymbol{\xi} \cdot \nabla T_{e0},$$

where $\boldsymbol{\xi}$ is the plasma displacement. We have verified that the inclusion of non-adiabatic electron response does not change significantly the radial structure of the $\delta T_e/T_{e0}$. We focus on the $n = 3$ BAE and the $n = 6$ LFM in this section, as they are two most unstable modes observed in the experiment [17].

One can find from figures 13(a) and (b) that radial structures of BAE and LFM from linear simulations agree qualitatively with ECE measurements, especially the radial location and mode width for both the LFM and the BAE. For reference, the BAE and the LFM in the ECE measurements are distinguished by their frequencies. Figure 13(c) shows the mode structure of the $n = 6$ LFM for each poloidal harmonic from the linear simulation. We would like to warn readers, however, that it is a nonlinearly evolving mode that we measure in experiments. It suggests further nonlinear simulations as a follow-up work for more precise comparison with experimental measurements.

Linear GTC simulations find that the frequency of the $n = 3$ BAE in the plasma frame is 56.6 kHz with the classical fast ion profile, and is 73.5 kHz with the relaxed fast ion profile. The experimental $m = 4$, $n = 3$ BAE occurs around 1215 ms when $q_{\min}$ from EFIT is ∼1.30 and has a frequency in the laboratory frame of $f_{\rm lab} = 106$ kHz, although the mode actually chirps rapidly about 10% in frequency [18]. Since the toroidal rotation at the peak of the eigenfunction is $f_{\rm rot} = 8.5$ kHz, the estimated BAE frequency in the plasma frame $f_{\rm plasma} = f_{\rm lab} - nf_{\rm rot}$ is ∼81 kHz is considerably higher than the simulated frequency and closer to the accumulation point of the Alfven continuum (figure 3). Figure 10 provides a likely explanation for this discrepancy. In the experiment, anisotropic population of co-passing tangential beams drives the instability but the simulations use an isotropic distribution function. As figure 10 shows, stronger fast-ion drive raises the computed mode frequency. Perhaps simulations with a more realistic distribution function will find better agreement with the measured frequency but that is left for future work.

For the LFM, GTC finds a frequency in the plasma frame of 26.9 kHz. The experimental $n = 6$ LFM occurs around 1183 ms when $q_{\min}$ from the EFIT is ∼1.33 and has a frequency in the laboratory frame of $f_{\rm lab} = 38$ kHz. Using $f_{\rm plasma} = f_{\rm lab} - nf_{\rm rot}$, this implies a plasma frame frequency of −3 kHz (in the electron direction), with an uncertainty of ∼5 kHz [17]. In contrast to the BAE, the LFM simulated frequency is higher than the frequency inferred from the experiment. One source of uncertainty in this comparison comes from the estimations of the Doppler shift of the mode frequencies. An oft-used approximation of the Doppler shift [32, 33] is $n\omega_\phi$, where ω_ϕ is the toroidal rotation angular frequency. However, finite equilibrium poloidal flow, together with finite pressure, contributes to radial electric field in the radial force balance. Therefore, it can make a difference of the true Doppler shift from its simple estimation $n\omega_\phi$. Note that current simulations use a local Maxwellian as an approximation to the neoclassical distribution function, thus neglect all neoclassical flows. Therefore, there exists uncertainty also from the simulation side, which can enlarge difference of estimated frequencies from the simulations and experiments, especially for the LFM.

A striking feature in the experiment is the strong dependence of BAE and LFM stabilities on relatively modest

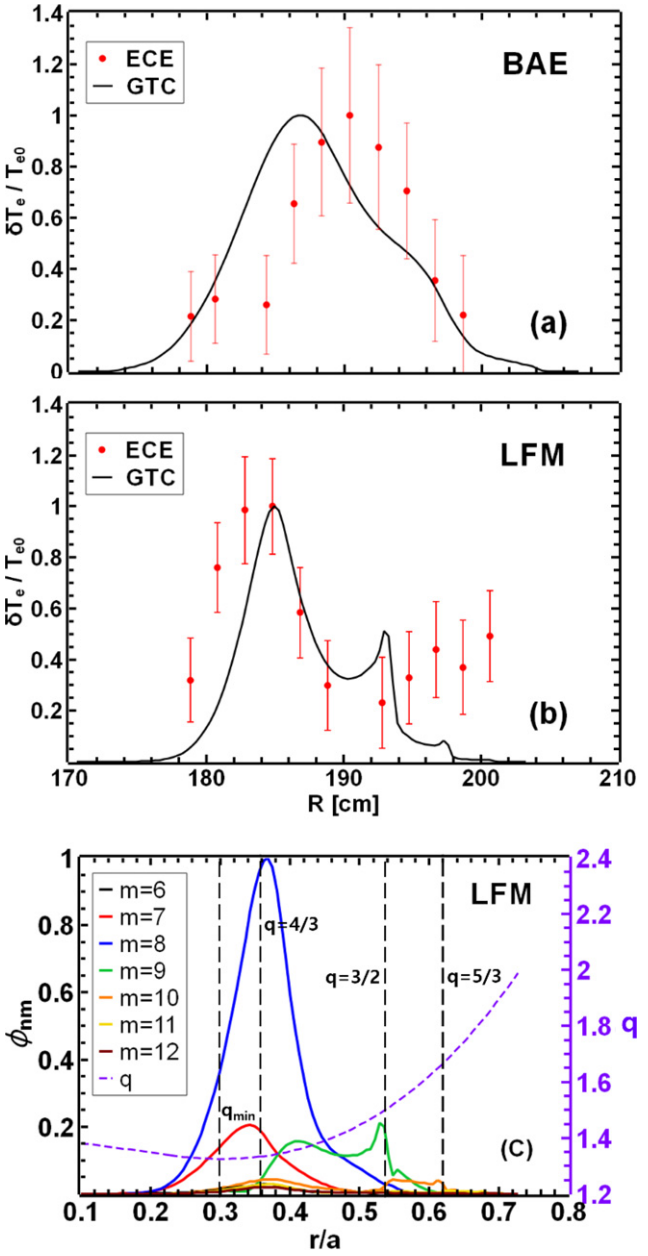

Figure 13. Radial profiles of perturbed electron temperature of (a) BAE and (b) LFM, obtained from GTC simulations (black) and ECE measurements (red). Panel (c) is radial structures of poloidal harmonics of the $n = 6$ LFM, together with q-profile. They are normalized by maximal value of the main poloidal harmonic.

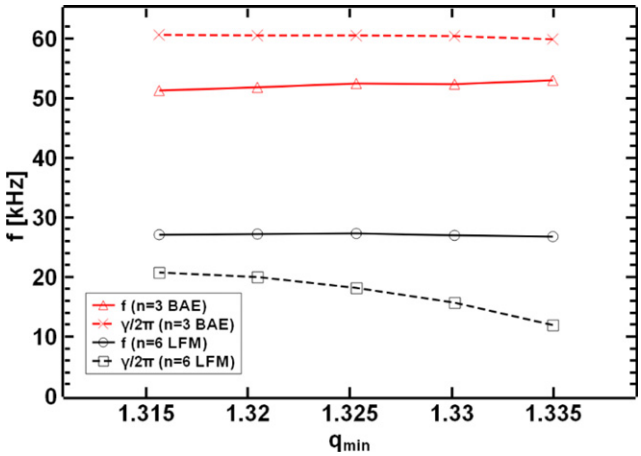

Figure 14. $q_{\min}$ scan of frequency (solid line) and linear growth rate (dashed line) of $n = 3$ BAE (red) and $n = 6$ LFM (black) by shifting overall value of q-profile from the reference case ($q_{\min} = 1.325$).

changes in the q-profile. For example, the $n = 3$ BAE persists about 30 ms, while the $n = 6$ LFM is only unstable for a few milliseconds. In 30 ms, $q_{\min}$ only changes by $\sim$0.03 so the BAE stability and especially the LFM stability is extremely sensitive to q. Figure 14 shows the simulated dependence on the $q_{\min}$ for the mode frequencies and growth rates. The dependence on $q_{\min}$ for the BAE is weaker than the experiment, although this discrepancy may also be caused by the use of an isotropic distribution function, as the experimental analysis suggests that the dependence of the resonant frequency of the injected co-passing ions on the $q_{\min}$ is the dominant factor determining the mode stability [18]. For the LFM, the simulations do show a significant dependence of the growth rate on $q_{\min}$, although the dependence is still weaker than that suggested by the experimental 'Christmas light' pattern of modes that only appear when $q_{\min}$ approaches a rational value [17].

7. Conclusion

In this work, we find both unstable BAE and LFM from GTC linear gyrokinetic simulations of the DIII-D shot #178631. The simulations find that the LFM is an interchange-type electromagnetic mode, and has several features similar to the LFM observed in the DIII-D experiments and the theoretical interpretation presented in reference [17]:

(a) It is excited even without fast ions.
(b) The mode structure is localized to the $q_{\min}$ and, compared to the BAE, the peak is closer to the $q_{\min}$, as in experiment [18]. Also, as in the experiment, the mode phase depends strongly on radius.
(c) As in the experiment, the frequency is in the range of the ion diamagnetic frequency but is somewhat higher than that suggested by the experiment.
(d) Instability is found over the same range of toroidal mode numbers as observed experimentally.
(e) As in the experiment, high electron temperature is strongly destabilizing but increasing ion temperature is stabilizing.
(f) Like the experiment, the calculated growth rate is sensitive to the $q_{\min}$ but the dependence appears weaker than that in the experiment.

The simulated BAE also has several features that resemble experiment.

(a) The mode stability is a strong function of fast-ion parameters. In the linear simulations, the mode frequency depends on the fast-ion density and temperature. This differs from the experiment, but the experimental observation of rapid frequency chirping suggests that the mode frequency is sensitive to the fast-ion population.
(b) The mode structure peaks near the $q_{\min}$ but shifts in position depending upon the $q_{\min}$ and the fast-ion parameters. Similar variation in the peak of the BAE eigenfunction is observed experimentally. Also, for both simulation and experiment, the phase of the mode varies with the radius.
(c) Unlike the experiment, the simulated frequency is well below the BAE accumulation frequency.
(d) Unstable toroidal modes are predicted over the same range as that observed experimentally.
(e) The dependence of the BAE stability on the ion temperature is weak in both simulation and experiment.
(f) Unlike in the experiment, the simulated growth rate depends only weakly on the $q_{\min}$.

The BAE and LFM from linear GTC simulations have the following common features: overall polarization is close to Alfvénic, but the sidebands have significant acoustic component. Parallel current drive is very weak and trapped electrons are stabilizing. Parallel magnetic compression is strongly destabilizing.

The simulated BAE and LFM also have distinct features. First, the main drive is wave–fast ion resonance for the BAE, while it is non-resonant interchange drive for the LFM. The sidebands of the LFM have stronger acoustic component than the BAE. While BAE shows a triangular mode structure, LFM has an elliptic shape.

Further linear simulations with anisotropic slowing-down fast ion distribution function to study beam angle-dependence of the BAE excitation, and nonlinear simulations to study BAE and LFM saturation and fast and thermal ion transport will be performed in the near future.

Acknowledgments

We would like to thank to A. Bierwage, Liu Chen, N. Gorelenkov, J.S. Kang, P. Lauber and D.A. Spong for helpful discussions. This work is supported by U.S. Department of Energy (DOE) SciDAC project ISEP and used resources of the Oak Ridge Leadership Computing Facility at Oak Ridge National Laboratory (DOE Contract No. DE-AC05-00OR22725) and the National Energy Research Scientific Computing Center (DOE Contract No. DE-AC02-05CH11231). This work is partially based upon work using

the DIII-D National Fusion Facility, a DOE Office of Science user facility, under Awards DE-FC02-04ER54698. This report was prepared as an account of work sponsored by an agency of the United States Government. Neither the United States Government nor any agency thereof, nor any of their employees, makes any warranty, express or implied, or assumes any legal liability or responsibility for the accuracy, completeness, or usefulness of any information, apparatus, product, or process disclosed, or represents that its use would not infringe privately owned rights. Reference herein to any specific commercial product, process, or service by trade name, trademark, manufacturer, or otherwise, does not necessarily constitute or imply its endorsement, recommendation, or favoring by the United States Government or any agency thereof. The views and opinions of authors expressed herein do not necessarily state or reflect those of the United States Government or any agency thereof.

Appendix A

In this appendix, we present a more precise ordering for $\delta B_\parallel/\delta B_\perp$ beyond a typical ordering $\left|\delta B_\parallel\right| / \left|\delta B_\perp\right| \sim \mathcal{O}(\beta)$. The first order perpendicular force balance in the long wavelength limit yields

$$\frac{\delta B_\parallel}{B_0} \simeq -\frac{4\pi}{B_0^2}\delta p. \tag{A1}$$

Note that general pressure perturbation is [58]

$$\delta p = -\boldsymbol{\xi}\cdot\nabla P_0 + \delta p_{\mathrm{comp}}. \tag{A2}$$

The first and the second terms in rhs of equation (A2) are the incompressible and compressible parts, respectively. Then, we take an ordering assuming that the contribution from the incompressible part is comparable to the total pressure perturbation

$$\left|\delta p\right| \sim \left|\boldsymbol{\xi}_\perp\cdot\nabla P_0\right|. \tag{A3}$$

From perpendicular component of the induction equation,

$$\frac{\left|\delta \mathrm{B}_\perp\right|}{B_0} \sim \left|k_\parallel\right|\left|\xi_\perp\right|. \tag{A4}$$

Combining equations (A1), (A3) and (A4), we finally get the following ordering.

$$\frac{\left|\delta B_\parallel\right|}{\left|\delta \mathrm{B}_\perp\right|} \sim \frac{4\pi P_0'}{B_0^2\left|k_\parallel\right|} \sim \frac{\beta}{L_p\left|k_\parallel\right|} \gg \mathcal{O}(\beta). \tag{A5}$$

Note that $\left|k_\parallel\right| \ll 1/qR_0$ near the mode rational surface for the interchange-type mode structure, and therefore it can lead to $\left|\delta B_\parallel\right| / \left|\delta \mathrm{B}_\perp\right| \sim \mathcal{O}(1)$ for BAE and LFM from linear GTC simulations. Note that equation (A5) can also be obtained from GTC formulation. With small parallel electric field, one can rewrite incompressible pressure response as

$$\delta p_{\mathrm{incomp}} = -\boldsymbol{\xi}\cdot\nabla P_0 \simeq P_0'\delta\psi. \tag{A6}$$

Here, $\delta\psi$ is the perturbed poloidal magnetic flux. In appendix B, we discuss more on this. Substituting equation (A6) into equation (A1), with $|\delta p| \sim |\delta p_{incomp}|$, we have

$$\frac{\left|\delta B_\parallel\right|}{B_0} \sim \frac{\beta}{\left|\nabla\psi\right| L_p}\delta\psi. \tag{A7}$$

Also in GTC, we use the following approximate expression for the perturbed perpendicular magnetic field [59].

$$\delta \mathrm{B}_\perp \simeq \nabla\delta\psi\times\nabla\alpha + \nabla\psi\times\nabla\delta\alpha. \tag{A8}$$

Taking $\nabla\boldsymbol{\psi}\cdot$ to equation (A8), we have

$$\nabla\psi\cdot\delta \mathrm{B}_\perp \simeq \mathrm{B}_0\cdot\nabla\delta\psi, \tag{A9}$$

which leads to

$$\frac{\left|\delta \mathrm{B}_\perp\right|}{B_0} \sim \frac{\left|k_\parallel\right|}{\left|\nabla\psi\right|}\delta\psi. \tag{A10}$$

From equations (A7) and (A10), we finally obtain the same ordering with equation (A5).

Appendix B

In this appendix, we present explicit expressions of energy exchange rates, denoted by shorthand notations in the main body, and details of the interchange-type energy exchange rate which is used as an estimation of ideal MHD-like pressure drive. In equation (2), the complete expression of energy exchange rate, the first and the second terms in rhs correspond to the perpendicular and parallel channels, respectively. We further decompose each channel into each species as follows

$$\mathrm{s}_\perp = e_\mathrm{s}\langle\langle \mathbf{v}_{\perp\mathrm{s}}\cdot\mathbf{E}_\perp\rangle_\mathrm{v}\rangle, \tag{B1}$$

$$\mathrm{s}_\parallel = e_\mathrm{s}\langle\langle v_{\parallel\mathrm{s}}E_\parallel\rangle_\mathrm{v}\rangle. \tag{B2}$$

Here, s = i, e and f correspond to thermal ion, electron and fast ion, respectively. As explained in section 4, $\langle\cdots\rangle_\mathrm{v}$ is a velocity space integral weighted by the perturbed distribution function.

In GTC, we use fluid-kinetic hybrid electron model, where the electron perturbed distribution function is separated into the adiabatic part and the non-adiabatic part [59]. The velocity space integration in equations (B1) and (B2) can thus be separated into two components. The adiabatic electron response gives rise to an interchange-type energy exchange rate s_{ic}. That is,

$$\mathrm{s}_{\mathrm{ic}} = \langle P_{\mathrm{s}0}'\delta\psi\left(\frac{\mathbf{b}_0\times\nabla B_0}{B_0^2} + \frac{\nabla\times\mathbf{b}_0}{B_0}\right)\cdot\nabla\phi\rangle, \tag{B3}$$

where the dominant component of the electron pressure perturbation corresponds to the incompressible ideal MHD pressure perturbation,

$$\delta P_{\mathrm{s,incomp}} = P_{\mathrm{s}0}'\delta\psi. \tag{B4}$$

Here, $\delta\psi$ is the perturbed poloidal magnetic flux and the subscript s represents electron species. The subdominant components of the electron pressure perturbation include the electron density perturbation and compressible magnetic perturbation. On the other hand, the resonant energy exchange $\mathrm{e}_{\perp,\mathrm{na}}$, $\mathrm{e}_{\parallel,\mathrm{na}}$ can be calculated using the non-adiabatic electron

response in equations (B1) and (B2). The total wave–electron energy exchange rate is the sum of $e_{\perp,na}$, $e_{\parallel,na}$ and e_{ic} in figure 8.

We note that this total wave–electron energy exchange rate is consistent with the conventional calculation of the interchange drive. We rewrite equation (B1) with gyrofluid moments [45, 60, 61] as follows

$$s_\perp = \langle \left(\delta P_{\perp s} \frac{\mathbf{b}_0 \times \nabla B_0}{B_0^2} + \delta P_{\parallel s} \frac{\nabla \times \mathbf{b}_0}{B_0} \right) \cdot \nabla \phi \rangle. \quad \text{(B5)}$$

Note that the perpendicular and parallel gyrocenter pressures

$$\delta P_{\perp s} \equiv \int d^3 V \mu B_0 \delta f_s, \qquad \delta P_{\parallel s} \equiv \int d^3 V m_s v_\parallel^2 \delta f_s, \quad \text{(B6)}$$

contain both resonant and non-resonant responses [62]. The non-resonant (adiabatic) response includes the dominant incompressible component of equation (B4) and the subdominant compressible components.

ORCID iDs

G.J. Choi https://orcid.org/0000-0003-0044-1650
X.S. Wei https://orcid.org/0000-0001-7486-0407
J.H. Nicolau https://orcid.org/0000-0003-1470-1820
W.L. Zhang https://orcid.org/0000-0002-7136-2119
W.W. Heidbrink https://orcid.org/0000-0002-6942-8043

References

[1] Chen L. and Zonca F. 2016 *Rev. Mod. Phys.* **88** 015008
[2] Todo Y. 2018 *Rev. Mod. Plasma Phys.* **3** 1
[3] Cheng C.Z., Chen L. and Chance M.S. 1985 *Ann. Phys.* **161** 21
[4] Cheng C.Z. and Chance M.S. 1986 *Phys. Fluids* **29** 3695
[5] Heidbrink W.W., Strait E.J., Chu M.S. and Turnbull A.D. 1993 *Phys. Rev. Lett.* **71** 855
[6] Turnbull A.D., Strait E.J., Heidbrink W.W., Chu M.S., Duong H.H., Greene J.M., Lao L.L., Taylor T.S. and Thompson S.J. 1993 *Phys. Fluids* B **5** 2546
[7] Gorelenkov N.N., Berk H.L., Fredrickson E. and Sharapov S.E. (JET EFDA Contributors) 2007 *Phys. Lett.* A **370** 70
[8] Gorelenkov N.N. *et al* 2007 *Plasma Phys. Control. Fusion* **49** B371
[9] Gorelenkov N.N. *et al* 2009 *Phys. Plasmas* **16** 056107
[10] Heidbrink W.W., Ruskov E., Carolipio E.M., Fang J., van Zeeland M.A. and James R.A. 1999 *Phys. Plasmas* **6** 1147
[11] Chavdarovski I. and Zonca F. 2009 *Plasma Phys. Control. Fusion* **51** 115001
[12] Chavdarovski I. and Zonca F. 2014 *Phys. Plasmas* **21** 052506
[13] Lauber P. 2013 *Phys. Rep.* **533** 33
[14] Zonca F., Chen L. and Santoro R.A. 1996 *Plasma Phys. Control. Fusion* **38** 2011
[15] Chen L. and Zonca F. 2007 *Nucl. Fusion* **47** S727
[16] Curran D., Lauber P., Carthy P.J.M., Graça S.d. and Igochine V. 2012 *Plasma Phys. Control. Fusion* **54** 055001
[17] Heidbrink W.W. *et al* 2021 *Nucl. Fusion* **61** 016029
[18] Heidbrink W.W. *et al* 2021 Stability of beta-induced Alfven eigenmodes (BAE) in DIII-D *Nucl. Fusion* **61** private communication
[19] Lin Z. 1998 *Science* **281** 1835
[20] Spong D.A. *et al* 2012 *Phys. Plasmas* **19** 082511
[21] Wang Z., Lin Z., Holod I., Heidbrink W.W., Tobias B., Van Zeeland M. and Austin M.E. 2013 *Phys. Rev. Lett.* **111** 145003
[22] Taimourzadeh S. *et al* 2019 *Nucl. Fusion* **59** 066006
[23] Zhang H.S., Lin Z., Holod I., Wang X., Xiao Y. and Zhang W.L. 2010 *Phys. Plasmas* **17** 112505
[24] Zhang H.S., Lin Z. and Holod I. 2012 *Phys. Rev. Lett.* **109** 025001
[25] Cheng J., Zhang W., Lin Z., Holod I., Li D., Chen Y. and Cao J. 2016 *Phys. Plasmas* **23** 052504
[26] Zhang H.S., Liu Y.Q., Lin Z. and Zhang W.L. 2016 *Phys. Plasmas* **23** 042510
[27] Liu Y., Lin Z., Zhang H. and Zhang W. 2017 *Nucl. Fusion* **57** 114001
[28] Cheng J., Zhang W., Lin Z., Li D., Dong C. and Cao J. 2017 *Phys. Plasmas* **24** 092516
[29] Chen Y., Zhang W., Cheng J., Lin Z., Dong C. and Li D. 2019 *Phys. Plasmas* **26** 102507
[30] Lin Z., Nishimura Y., Xiao Y., Holod I., Zhang W.L. and Chen L. 2007 *Plasma Phys. Control. Fusion* **49** B163
[31] Bao J., Lin Z. and Lu Z.X. 2018 *Phys. Plasmas* **25** 022515
[32] Hahm T.S. and Tang W.M. 1994 *Phys. Plasmas* **1** 2099
[33] Wong K.L., Bretz N.L., Hahm T.S. and Synakowski E. 1997 *Phys. Lett.* A **236** 339
[34] Dong G., Bao J., Bhattacharjee A., Brizard A., Lin Z. and Porazik P. 2017 *Phys. Plasmas* **24** 081205
[35] Xiao Y., Holod I., Wang Z., Lin Z. and Zhang T. 2015 *Phys. Plasmas* **22** 022516
[36] Lao L.L., John H.S., Stambaugh R.D., Kellman A.G. and Pfeiffer W. 1985 *Nucl. Fusion* **25** 1611
[37] Ongena J.P.H.E., Voitsekhovitch I., Evrard M. and McCune D. 2012 *Fusion Sci. Technol.* **61** 180
[38] Pankin A., McCune D., Andre R., Bateman G. and Kritz A. 2004 *Comput. Phys. Commun.* **159** 157
[39] Deng W., Lin Z., Holod I., Wang Z., Xiao Y. and Zhang H. 2012 *Nucl. Fusion* **52** 043006
[40] Tobias B.J., Classen I.G.J., Domier C.W., Heidbrink W.W., Luhmann N.C., Nazikian R., Park H.K., Spong D.A. and Van Zeeland M.A. 2011 *Phys. Rev. Lett.* **106** 075003
[41] Ma R., Zonca F. and Chen L. 2015 *Phys. Plasmas* **22** 092501
[42] Lu Z.X., Wang X., Lauber P. and Zonca F. 2018 *Nucl. Fusion* **58** 082021
[43] Chu M.S., Greene J.M., Lao L.L., Turnbull A.D. and Chance M.S. 1992 *Phys. Fluids* B **4** 3713
[44] Kramer G.J., Cheng C.Z., Podestà M. and Nazikian R. 2020 *Plasma Phys. Control. Fusion* **62** 075012
[45] Brizard A.J. and Hahm T.S. 2007 *Rev. Mod. Phys.* **79** 421
[46] Cheng C.Z., Kramer G.J., Podesta M. and Nazikian R. 2019 *Phys. Plasmas* **26** 082508
[47] Sugama H. 2000 *Phys. Plasmas* **7** 466
[48] Brizard A.J. 2000 *Phys. Plasmas* **7** 4816
[49] Zonca F., Biancalani A., Chavdarovski I., Chen L., Troia C.D. and Wang X. 2010 *J. Phys.: Conf. Ser.* **260** 012022
[50] Jackson J.D. 1999 *Classical Electrodynamics* 3rd edn (New York: Wiley)
[51] Deng W., Lin Z. and Holod I. 2012 *Nucl. Fusion* **52** 023005
[52] McClenaghan J., Lin Z., Holod I., Deng W. and Wang Z. 2014 *Phys. Plasmas* **21** 122519
[53] Berk H.L. and Dominguez R.R. 1977 *J. Plasma Phys.* **18** 31
[54] Tang W.M., Connor J.W. and Hastie R.J. 1980 *Nucl. Fusion* **20** 1439
[55] Joiner N., Hirose A. and Dorland W. 2010 *Phys. Plasmas* **17** 072014
[56] Zonca F. and Chen L. 2014 *Phys. Plasmas* **21** 072120
[57] Zonca F. and Chen L. 2014 *Phys. Plasmas* **21** 072121
[58] Chen L. and Zonca F. 2017 *Phys. Plasmas* **24** 072511

[59] Holod I., Zhang W.L., Xiao Y. and Lin Z. 2009 *Phys. Plasmas* **16** 122307
[60] Brizard A. 1992 *Phys. Fluids* B **4** 1213
[61] Liu P., Zhang W., Dong C., Lin J., Lin Z., Cao J. and Li D. 2017 *Phys. Plasmas* **24** 112114
[62] Biglari H. and Chen L. 1991 *Phys. Rev. Lett.* **67** 3681